JGR Solid Earth

RESEARCH ARTICLE
10.1029/2025JB032001

Crustal Structure and Seismogenic Environment for the January 2025 Mw 7.1 Southern Tibet (Dingri) Earthquake

Bingfeng Zhang[1], He Tan[1,2], Xiao Xiao[1], Dongdong Wang[1], Yiming Bai[1], Tianjue Li[1], Shijie Hao[1], Jing Chen[1], Jiayuan Yao[3], Xuewei Bao[4], and Ping Tong[1,5]

[1]Division of Mathematical Sciences, School of Physical and Mathematical Sciences, Nanyang Technological University, Singapore, Singapore, [2]State Key Laboratory of Earthquake Dynamics and Forecasting, Institute of Geology, China Earthquake Administration, Beijing, China, [3]Hubei Subsurface Multi-scale Imaging Key Laboratory, School of Geophysics and Geomatics, China University of Geosciences, Wuhan, China, [4]Key Laboratory of Geoscience Big Data and Deep Resource of Zhejiang Province, School of Earth Sciences, Zhejiang University, Hangzhou, China, [5]Earth Observatory of Singapore, Nanyang Technological University, Singapore, Singapore

Abstract On 7 January 2025, a M_w 7.1 normal-faulting earthquake occurred in the Dinggye Rift zone, southern Tibetan plateau. In this study, we present high-resolution crustal S-wave isotropic and P-wave azimuthally anisotropic velocity models around the source region of this earthquake, constructed using novel adjoint-state traveltime tomography techniques. We find that the high-slip zone of the mainshock rupture coincides with a high-strength asperity (Lhagai gneiss dome) characterized by negligible seismic anisotropy. The source region is subject to basal shear imposed by the underthrusting Indian slab and impinging fluid flow through a slab window, as evidenced by the observations of convergence-parallel anisotropy and pronounced low-velocity anomalies below the hypocenter. These tectonic forces collectively reconfigure the local stress field to favor normal faulting by counteracting the convergence-induced compression, and together with the high elastic strain accumulation facilitated by the fault asperity, contributes to the generation of this high-magnitude normal-faulting continental earthquake.

Plain Language Summary Timely illumination of seismogenic environment for large earthquakes is crucial for understanding their genesis and for formulating disaster mitigation policies in earthquake-prone regions. In this study, we present high-resolution images of the subsurface crustal structures in the source region of the 2025 M_w 7.1 Southern Tibet earthquake, derived from comprehensive analyses of seismic records. The results reveal that the high magnitude of this devastating earthquake is because it ruptured an anomalously high-strength geological unit. The normal-faulting rupture behavior is driven by the combined effect of several deep-seated geodynamic processes, including plate subduction and fluid upwelling.

Key Points:

- We present 3-D crustal P- and S-wave velocity models of the 2025 M_w 7.1 Southern Tibet earthquake source region and its surroundings
- The large-magnitude earthquake is attributed to the failure of a high-strength fault asperity at the Lhagai gneiss dome
- The development of seismogenic normal fault is facilitated by deep-seated geodynamic processes, including basal shear and fluid upwelling

Supporting Information:

Supporting Information may be found in the online version of this article.

Correspondence to:

P. Tong,
tongping@ntu.edu.sg

Citation:

Zhang, B., Tan, H., Xiao, X., Wang, D., Bai, Y., Li, T., et al. (2025). Crustal structure and seismogenic environment for the January 2025 Mw 7.1 southern Tibet (Dingri) earthquake. *Journal of Geophysical Research: Solid Earth*, *130*, e2025JB032001. https://doi.org/10.1029/2025JB032001

Received 15 MAY 2025
Accepted 24 OCT 2025
Corrected 17 NOV 2025

This article was corrected on 17 NOV 2025. See the end of the full text for details.

Author Contributions:

Conceptualization: Bingfeng Zhang, Ping Tong
Data curation: Bingfeng Zhang
Formal analysis: Bingfeng Zhang, He Tan
Funding acquisition: Ping Tong
Investigation: Bingfeng Zhang
Methodology: Shijie Hao, Jing Chen, Ping Tong
Project administration: Ping Tong
Software: Bingfeng Zhang, Shijie Hao, Jing Chen, Ping Tong

1. Introduction

On 7 January 2025, a devastating M_w 7.1 (M_s 6.8) earthquake struck Dingri County, Xizang Autonomous Region, China, causing more than 126 fatalities and damaging over 27,200 buildings. The mainshock hypocenter and centroid were located at 87.45°E, 28.50°N, 10-km depth and 87.47°E, 28.56°N, 12-km depth, respectively, according to the CENC (China Earthquake Networks Center) and GCMT (Global Centroid Moment Tensor) reports (Figure 1). This earthquake occurred along the Dengme Co fault, with ~3 m coseismic vertical offsets visible on the surface (Xu, Wang et al., 2025), manifesting as a northward-propagating unilateral rupture (rupture length: ~50–80 km; duration: ~27 s). Field surveys, seismic waveform inversions, and InSAR analyses indicate that it was a normal-faulting earthquake with minor left-lateral strike-slip component (strike: ~187°; dip: ~40–50°; e.g., Wang, Li et al., 2025). More than 30,000 aftershocks have been detected (Yao et al., 2025), including an M_b 5.1 and an M_b 5.0 event. Notably, regional seismicity has significantly increased following the 2015 M_w 7.8 Gorkha–Nepal earthquake that occurred ~250 km to the southwest (L. Li et al., 2017), remotely triggering the 2015 M_w 5.8, 2016 M_w 5.3, and 2020 M_w 5.7 earthquakes. The 2025 M7.1 Dingri mainshock is the largest Tibetan normal-faulting earthquake in recent years and is among the world's largest continental normal-faulting earthquakes on record. Deciphering its seismogenic environment is crucial for future disaster mitigation in this earthquake-prone area and for advancing knowledge of the mechanisms responsible for generating large normal-faulting earthquakes.

Supervision: Ping Tong
Validation: Bingfeng Zhang
Visualization: Bingfeng Zhang
Writing – original draft: Bingfeng Zhang
Writing – review & editing: Bingfeng Zhang, Xiao Xiao, Dongdong Wang, Yiming Bai, Tianjue Li, Shijie Hao, Jiayuan Yao, Xuewei Bao, Ping Tong

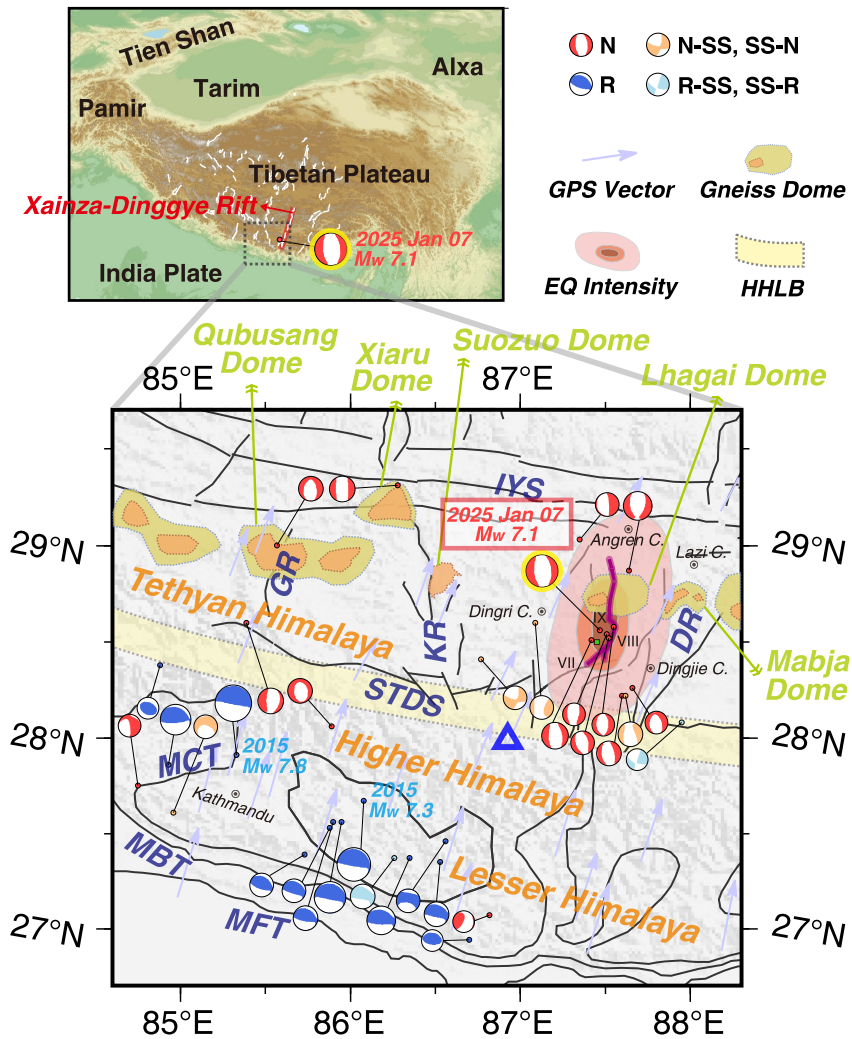

Figure 1. Tectonic settings of the study region. The epicenter (green square; from CENC) and intensity map (from the China Earthquake Administration) of the M7.1 Dingri mainshock, the locations of the leucogranite-cored northern Himalayan gneiss domes and the Higher Himalayan leucogranite belt (Fan et al., 2021; Zeng et al., 2011), the focal mechanisms of the mainshock and historical events (from GCMT), and the GPS velocities relative to stable Eurasia (Wang & Shen, 2020) are shown. Fault traces (black solid lines) are primarily from the China Active Faults Database and modified after X. Xu et al. (2025), with the seismogenic Dengme Co fault highlighted in purple. Mount Everest is indicated by the blue triangle. In the top inset, the Tibetan normal faults are represented by white lines. Abbreviations: DR, Dinggye Rift; KR, Kung Co Rift; GR, Gyirong Rift; MFT, Main Frontal Thrust; MBT, Main Boundary Thrust; MCT, Main Central Thrust; STDS, South Tibetan Detachment System; IYS, Indus–Yarlung Suture; R, Reverse; N, Normal; SS, Strike-Slip; HHLB, Higher Himalayan Leucogranite Belt.

The west-dipping Dengme Co fault (i.e., the seismogenic fault) serves as one of the graben-bounding faults in the southern part of the Xainza–Dinggye Rift zone (Figure 1). The development of the Xainza–Dinggye Rift zone, along with other rifts across the high plateau of Tibet, began in the Miocene (e.g., Dinggye: 13–11 Ma; Kali et al., 2010; J. Zhang & Guo, 2007). Rift kinematics has evolved over time and varies along strike (Bian et al., 2022). For instance, rift acceleration began at ~10–6 Ma in the Xainza rift zone (Hager et al., 2009) but only at ~6–4 Ma in the Dinggye Rift zone to the south (Kali et al., 2010). Several hypotheses have been proposed to explain the enigmatic Tibetan rifting and the associated normal-faulting earthquakes; however, their precise mechanisms remain a topic of intense debate. The contrasting rift morphologies between the northern and southern plateau have been attributed to the addition of north-directed basal shear stresses in the south (imposed by the underthrusting Indian plate), according to the numerical and analog modeling of surface tectonics (Copley et al., 2011; McCaffrey & Nabelek, 1998). Ductile channel flow within the middle–lower crust has been

hypothesized to be active beneath the Tibet (S. Huang et al., 2020), which could induce viscous buckling of the brittle upper crust and lead to east–west extension at shallow levels (Bischoff & Flesch, 2018). In addition, convective removal of the overthickened mantle lithosphere and its replacement by the upwelling asthenosphere may have pervasively occurred across the northern Tibet and locally in the south (Barazangi & Ni, 1982; J. Li & Song, 2018). Such processes would elevate the gravitational potential energy (GPE) and modify the regional stress field in a manner that promotes normal faulting (England & Houseman, 1989; England & Molnar, 1993).

Geologically, the Dengme Co fault is situated within the Tethyan Himalaya. The Tethyan Himalaya is predominantly covered by folded sedimentary successions deposited on the Indian continental margin during the Paleozoic–Eocene periods (Hodges, 2000), and is separated from the Higher Himalaya by the north-dipping South Tibetan Detachment System (STDS) that was once active at ∼25–15 Ma (F. Wu et al., 2015). The Higher Himalaya in the footwall of STDS represents the metamorphic core of the Himalaya, primarily composed of high-grade metasedimentary and meta-igneous rocks, along with the associated leucogranite bodies (Hodges, 2000). These metamorphic rocks are also exposed in the central Tethyan Himalaya as a series of bead-like gneiss domes (Figure 1). At the surface, the Dengme Co fault transects the Lhagai gneiss dome in its northern segment, while cutting through the Tethyan Himalayan sedimentary sequence in its southern segment.

Measuring seismic velocity and anisotropy properties of the solid Earth can provide insights into the structural heterogeneities, stress–strain fields, fluid migration and deep geodynamic processes that may be linked to earthquake nucleation. Numerous large-scale seismic tomographic models of the Tibetan plateau (e.g., Bao et al., 2015; M. Chen et al., 2017; S. Huang et al., 2020; Li, He et al., 2024; Liang et al., 2023; Ma et al., 2025; Yang et al., 2012) provide only first-order regional features of the Dingri earthquake source region. Existing regional-scale models primarily focus on the 2015 M_w 7.8 Gorkha–Nepal earthquake source region and generally lack constraints on seismic anisotropy (e.g., Bai et al., 2019; Lü et al., 2024; Pei et al., 2016; Thapa et al., 2023; Wei & Zhao, 2016). Knowledge of anisotropic properties mainly come from the sparse point measurements of shear-wave splitting analyses, which lacks depth resolution (e.g., Mohanty, 2023; B. Zhang et al., 2023; B. Zhang et al., 2025). To gain insights into the seismogenic environment of the M7.1 Dingri earthquake, we determine the crustal S-wave velocity, P-wave velocity and azimuthal anisotropy beneath the source region using our newly developed tomographic packages, SurfATT (Xu, Hao et al., 2025) and TomoATT (J. Chen et al., 2025).

2. Data and Methods

2.1. Ambient Noise Data

Vertical-component ambient noise data recorded by 26 broadband stations of the HIMNT Array (i.e., the 2001–2002 Himalayan Nepal Tibet Seismic Experiment; Schulte-Pelkum et al., 2005) are processed to retrieve inter-station empirical Green's functions following the methodology of Bensen et al. (2007). The main steps include: (a) segmentation and resampling of waveforms into hour-length segments (with 30-min overlapping) and at 5 Hz, (b) removal of instrument response, (c) band-pass filtering (2–60 s), (d) time- and frequency-domain whitening, (e) waveform cross-correlation between all synchronous stations, and (f) robust stacking of all hour-length inter-station cross-correlations (Pavlis & Vernon, 2010). Fundamental-mode Rayleigh-wave phase traveltimes in the period range of 3–45 s are measured by Automatic Frequency–Time Analysis. We then select high-quality traveltimes for subsequent surface-wave tomographic inversions based on the following criteria: (a) a minimum signal-to-noise ratio of 5, (b) an inter-station distance greater than one wavelength at that period, and (c) the removal of outliers that are more than two standard deviations away from the average. See Figure 2 for the statistics of the ambient noise data set.

2.2. SurfATT: Adjoint-State Surface-Wave Traveltime Tomography

We employ the topography-incorporated adjoint-state surface-wave traveltime tomography method (SurfATT; Hao, Chen, et al., 2024; M. Xu et al., 2025), a direct surface-wave inversion technique, to invert for isotropic shear-wave velocity $\beta(\boldsymbol{x})$ (i.e., $\boldsymbol{m}$) at 0–40 km depths. The principle of this method is to minimize the weighted frequency-dependent surface-wave traveltime misfits between observations $T^o_{f,i,j}$ and model predictions $T_{f,i,j}(\boldsymbol{m})$ for all frequencies ($f = 1, 2, \ldots, N_f$) and all station pairs ($i, j = 1, 2, \ldots, N_r$):

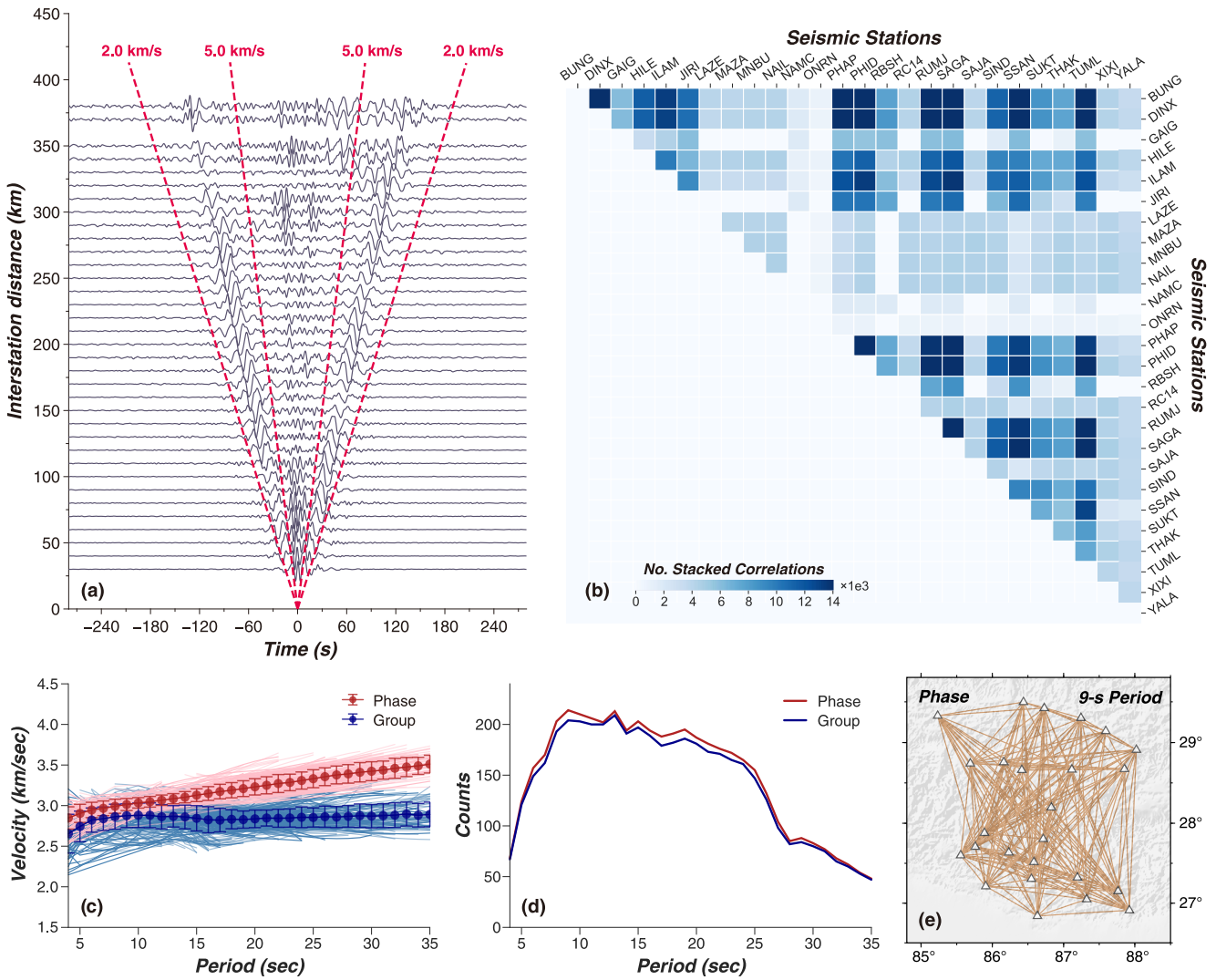

Figure 2. Ambient noise data set statistics. (a) Ambient-noise cross-correlations plotted as a function of inter-station distance and time lag. (b) Diagonal heatmap showing the numbers of hour-length inter-station cross-correlations used in the robust stacking procedure. (c) Rayleigh-wave group and phase velocity dispersion curves. Circles show the averages at different periods, with one standard deviation indicated by the bars. (d) The numbers of Rayleigh-wave group and phase velocity measurements at different periods. (e) Path coverage at 9-s period for Rayleigh-wave phase velocity measurements. HIMNT stations are represented by triangles.

$$\min_{\boldsymbol{m}} \chi(\boldsymbol{m}) = \sum_{f=1}^{N_f} \chi_f(\boldsymbol{m}) = \sum_{f=1}^{N_f} \sum_{i=1}^{N_r} \sum_{j=i}^{N_r} \frac{w_{f,i,j}}{2} \left(T_{f,i,j}(\boldsymbol{m}) - T^o_{f,i,j}\right)^2.$$

The Fréchet derivative $K_c^{\beta;\alpha,\rho}(\boldsymbol{x})$ of the misfit function with respect to 3-D shear-wave velocity $\beta(\boldsymbol{x})$ is calculated by combining the 2-D surface-wave kernel $K_f^s(\boldsymbol{x^0})$ with the 1-D depth kernels of surface-wave velocity c with respect to Vp, Vs, and density, respectively (i.e., $K_{c,f}^{\alpha}(\boldsymbol{x})$, $K_{c,f}^{\beta}(\boldsymbol{x})$, and $K_{c,f}^{\rho}(\boldsymbol{x})$):

$$K_c^{\beta;\alpha,\rho}(\boldsymbol{x}) = \left\{ \sum_{f=1}^{N_f} -K_f^s(\boldsymbol{x^0})\, s_f(\boldsymbol{x^0}) \left[K_{c,f}^{\alpha}(\boldsymbol{x}) \frac{d\alpha(\boldsymbol{x})}{d\beta(\boldsymbol{x})} + K_{c,f}^{\beta}(\boldsymbol{x}) + K_{c,f}^{\rho}(\boldsymbol{x}) \frac{d\rho(\boldsymbol{x})}{d\beta(\boldsymbol{x})} \right] \right\} \beta(\boldsymbol{x}),$$

where $s_f(\boldsymbol{x^0})$ is the surface-wave slowness calculated from $\beta(\boldsymbol{x})$ under the assumption of a horizontally homogeneous model; $d\alpha(\boldsymbol{x})/d\beta(\boldsymbol{x})$ and $d\rho(\boldsymbol{x})/d\beta(\boldsymbol{x})$ are the empirical relationships relating Vp and density to Vs Surface-wave traveltime fields and kernels on undulated topography are derived with high accuracy and

efficiency by solving anisotropic eikonal and adjoint equations using the fast-sweeping method (H. Zhao, 2004). The adjoint-state method solves adjoint equations and generates sensitivity kernels across the entire model domain. This property naturally addresses the multipathing phenomenon, in which the first arrival is influenced by the structure along multiple shortest paths (J. Chen et al., 2025; Tong et al., 2024). Without special treatments, ray-based methods identify only a single shortest path, thereby generating an incomplete sensitivity kernel. Model updating is handled by a step-size-controlled gradient descent algorithm. A multiple-grid model parameterization comprising five sets of staggered coarse grids and a kernel density normalization are employed in the inversion to enhance inversion reliability and to accelerate model convergence. We refer to Section 3.1 for the inversion parameters used and Hao, Chen et al. (2024) for more details of SurfATT.

2.3. First-Arrival P-Wave Traveltimes

A new local earthquake catalog (2001–2002) for the Dingri earthquake source region and its surroundings is constructed using the continuous three-component seismograms of the HIMNT array under the LOC-FLOW framework (M. Zhang et al., 2022). A deep neural network-based phase picker (PhaseNet) is employed to identify P and S phases, with the phase probability threshold set to be 0.5 (Zhu & Beroza, 2018). A grid search method (REAL) is then utilized to associate the machine learning-based phase picks with specific earthquakes (M. Zhang et al., 2019). The search intervals are set to be 0.1° horizontally and 2 km vertically, while the synthetic traveltimes are calculated based on the regional-average Vs profile derived from SurfATT. In total, we associate 1,472 earthquakes with 6,649 P and 4,794 S phases. We then implement VELEST (Kissling et al., 1994) to update the velocity model. In order to reduce the probabilities of false positives, strict thresholds of at least ten phases and an azimuthal gap less than 180° are required. We then use HYPOINVERSE (Klein, 2002) to refine the absolute event locations based on the updated model. The average root-mean-square traveltime residual of these events is 0.18 s. Hypocenter locations in earthquake clusters are further refined using the double-difference relative location method (HypoDD; Waldhauser & Ellsworth, 2000), incorporating both phase-arrival–based differential times and waveform cross-correlation–based differential times (FDTCC; M. Zhang et al., 2022). As a result, our AI-enhanced relocation workflow yields a total of 2,892 first P arrivals from 627 local events. A visual inspection is also conducted to assess the accuracy of the phase picks and to remove those considered ambiguous by the analysts. See Figure S1a in Supporting Information S1 for example, AI-picked first P arrivals. Note that we use S phases for constructing the earthquake catalog but not for tomographic inversion, for the additional ambiguity from S-wave splitting.

The AI-picked first P arrivals are then incorporated into a regional phase catalog consisting of hand-picked and publicly archived (ISC, CENC) Pg and Pn arrivals (Li, Pei, et al., 2024) to prepare the input data for tomographic inversions. This integrated data set is filtered based on the following selection criteria: (a) stations and events are restricted to the Dingri earthquake source region and its surroundings (84.9°–90.1°E, 26.3°–29.5°N); (b) focal depth is above 30 km; (c) only one event is retained in a block region of 0.05° × 0.05° × 4.0 km to reduce data redundancy; (d) each event is captured by at least three stations; (e) duplicate events are identified and filtered; (f) outlier traveltimes that are >3 s away from the time–distance linear regression lines are excluded (Figure S1b in Supporting Information S1); and (g) for Pg and Pn, the hypocentral distance is <120 km and >250 km, respectively, to ensure that the retained phases represent first P arrivals (Figure S1b in Supporting Information S1). A geographical weighting scheme (Ruan et al., 2019) is further applied to the data space to balance the unevenly distributed data in our study area (Figure 3). Additionally, to mitigate the influence of source term uncertainties on the tomographic inversions, we compute common-source differential traveltimes by catalog subtraction for station pairs that are <100 km apart and possess <30° angular difference to a common source. As a result, a total of 9,542 absolute traveltimes and 12,912 common-source differential traveltimes originating from 1,678 local earthquakes and recorded by 159 seismic stations are selected for subsequent body-wave tomographic inversions. See Figure 3 for the spatial distribution of local earthquakes and seismic stations involved in the P-wave data set.

2.4. TomoATT: Adjoint-State Body-Wave Traveltime Tomography

We employ the adjoint-state body-wave traveltime tomography method (TomoATT; J. Chen et al., 2023; J. Chen et al., 2025; Tong, 2021; Tong et al., 2024) to invert for P-wave slowness $s(\boldsymbol{x})$ and azimuthal anisotropy parameters $\xi(\boldsymbol{x})$, $\eta(\boldsymbol{x})$ at 0–20 km depths. The optimal model $\boldsymbol{m}$, described by $s(\boldsymbol{x})$, $\xi(\boldsymbol{x})$ and $\eta(\boldsymbol{x})$, is determined by minimizing the sum of weighted misfits for absolute and common-source differential traveltimes:

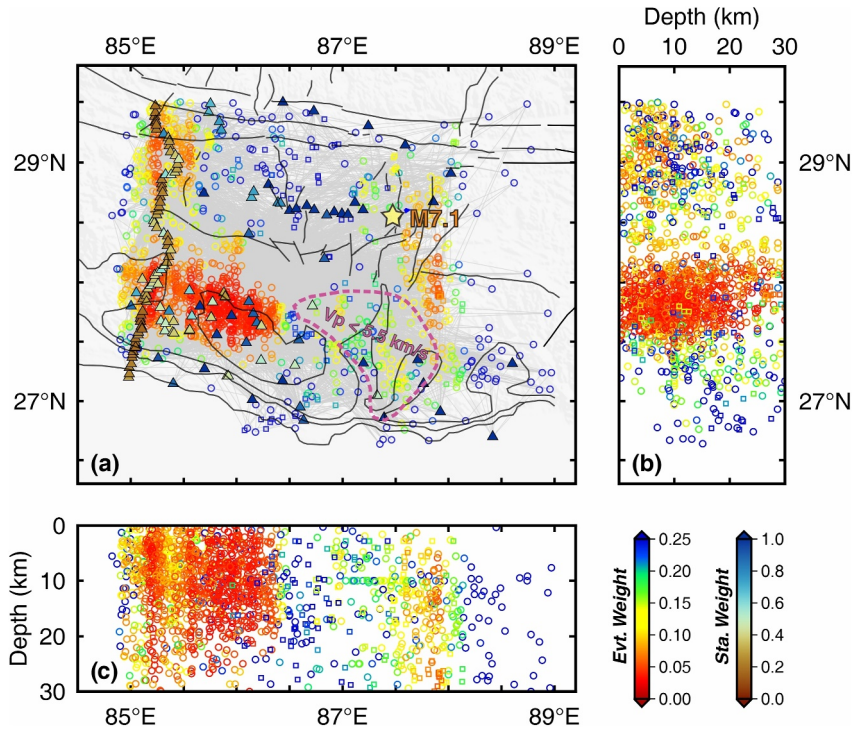

Figure 3. Spatial distribution of local earthquakes and seismic stations involved in the P-wave data set. (a) Horizontal section view. (b–c) Vertical section view along longitude and latitude directions. Local earthquakes are denoted by dots (J Li et al., 2024) or squares (AI-picked). Seismic stations are represented by triangles (Quantity: 159). Both symbols are color-coded by the weights assigned during the tomographic inversions, derived from geographical weighting. Each traveltime datum is depicted as a gray line connecting the associated local earthquake and seismic station. The M7.1 Dingri earthquake centroid location is indicated by yellow star. A low-Vp region (<5.5 km/s; L1) at 5-km depth is outlined in purple dashed line.

$$\min_{\boldsymbol{m}} \chi(\boldsymbol{m}) = \sum_{i=1}^{N_s} \sum_{j=1}^{N_r} \frac{w_{i,j}}{2} (T_{i,j}(\boldsymbol{m}) - T^o_{i,j})^2 + \sum_{i=1}^{N_s} \sum_{j=1}^{N_r} \sum_{k=1}^{N_r} \frac{w_{i,j,k}}{2} (\Delta T_{i,j,k}(\boldsymbol{m}) - \Delta T^o_{i,j,k})^2,$$

where $\Delta T_{i,j,k}$ and $\Delta T^o_{i,j,k}$ are synthetic and observed common-source differential traveltimes; i, j, and k denote the i-th event, j-th and k-th stations; N_s and N_r represent the numbers of events and stations.

The underlying logic for calculating traveltime fields, the Fréchet derivatives $K^s(\boldsymbol{x})$, $K^\xi(\boldsymbol{x})$, $K^\eta(\boldsymbol{x})$ of the misfit function with respect to $s(\boldsymbol{x})$, $\xi(\boldsymbol{x})$, and $\eta(\boldsymbol{x})$, the inversion scheme, and model regularization is the same as implemented in SurfATT. To mitigate the influence of source uncertainty on imaging results, the hypocenter and origin time are also iteratively updated during the inversion process using the gradient descend method. We refer to Section 3.2 for the inversion parameters and workflow used, and J. Chen et al. (2023) for more details of TomoATT.

3. Inversion Parameters and Checkerboard Resolution Tests

3.1. SurfATT: Inversion Parameters

The study area is discretized into a fine 3-D mesh with intervals of 0.05° × 0.05° × 2.5 km, on which the forward phase-traveltime field and adjoint field are computed. The size of the inversion grids is chosen based on the results of checkerboard tests (see Section 3.3), and we ensure that a one-wavelength anomaly is sampled by approximately five grid points to avoid spatial aliasing. A total of 4,274 high-quality Rayleigh-wave phase traveltimes between 252 station pairs within the period range of 4–35 s with 1 s increments are included in the inversion. A regional-average 1-D shear-wave velocity profile is utilized as the starting model for the 3-D inversion, which is

derived by inverting the average dispersion curve. Topography data incorporated into the forward modeling are sourced from the SRTM30 digital elevation model (https://topex.ucsd.edu/www_html/srtm30_plus.html). See Figure S2 in Supporting Information S1 for the illustrations of the initial model, depth sensitivity kernels, misfit function reduction, and traveltime residuals prior to and following the inversion.

3.2. TomoATT: Inversion Parameters and Workflow

The model domain is discretized into a fine 3-D mesh with intervals of 0.04° × 0.04° × 1.0 km, on which the forward P-traveltime field and adjoint field are computed. The horizontal size of the inversion grids is chosen based on the results of checkerboard tests (see Section 3.4) as in SurfATT, while a flexible inversion grid is employed in the depth direction. We utilize the optimal 1-D isotropic model derived from inverting the same data set as the initial model for subsequent 3-D inversions. The 1-D inversion begins with the regional-average Vp model of Li, Pei, et al. (2024).

The 3-D inversion workflow consists of three stages designed to reduce variable coupling: (a) we perform preliminary earthquake relocation using the 1-D initial model and update the source terms and associated traveltimes (only absolute traveltimes are used); (b) we simultaneously update the model and the source terms (both absolute and differential traveltimes are used); and (c) we perform additional earthquake relocation using the final 3-D model to obtain more accurate earthquake locations (only absolute traveltimes are used). See Figure S3 in Supporting Information S1 for the illustrations of the initial model, misfit function reduction, traveltime residuals, and event location changes through the inversion.

3.3. SurfATT: Checkerboard Resolution Tests

A series of checkerboard resolution tests is performed to evaluate the resolving ability of our data as well as the robustness of the surface-wave tomographic inversions. Two layers (0 km–15 km, 15 km–55 km) of smoothly alternating checkered perturbations with varying lateral cell sizes are established to mimic velocity anomalies of different scales within the upper crust and the mid–lower crust. Synthetic traveltimes are simulated using the target model and then deliberately contaminated by random Gaussian noise with a standard deviation of 0.1 s. Data configurations and inversion parameters are kept consistent with those used in the real-data inversion. The results demonstrate satisfactory recovery of ∼0.5°-wide velocity anomalies above 40-km depth in areas with descent data coverage, which includes the Dingri earthquake source region (Figure S4 in Supporting Information S1).

3.4. TomoATT: Checkerboard Resolution Tests

Checkerboard resolution and leakage tests are conducted to evaluate the resolving capability of our data, the robustness of the body-wave tomographic inversions, and the coupling effects of velocity and anisotropy. For the resolution test, two layers (0–10 km, 10–25 km) of smoothly alternating checkered perturbations with lateral cell sizes of ∼0.8° for velocity and ∼1.0° for anisotropy are established. Synthetic traveltimes are simulated using the target model and then deliberately contaminated by random Gaussian noise with a standard deviation of 0.05 s. Data configurations and inversion parameters are kept consistent with those used in the real-data inversion, except that earthquake locations are held fixed. In Figure S5 in Supporting Information S1, dashed lines outline the areas where both velocity and anisotropy anomalies are well recovered, which includes the Dingri earthquake source region. For the leakage test, all configurations are the same as those in the resolution test, except that no anisotropy is added to the target model (Figure S6 in Supporting Information S1). The satisfactory recovery of velocity anomalies and minor leakage from velocity to anisotropy in this test demonstrate that the anisotropy features delineated in this study are reliable. In Figure S7 in Supporting Information S1, we also present the checkerboard resolution test results in which earthquake locations are perturbed and jointly inverted for.

4. Results

According to the checkerboard resolution tests, shear-wave velocity at 0–40 km depths and P-wave velocity and anisotropy at 0–25 km depths can be well resolved by our tomographic inversions, which are presented in the following sections.

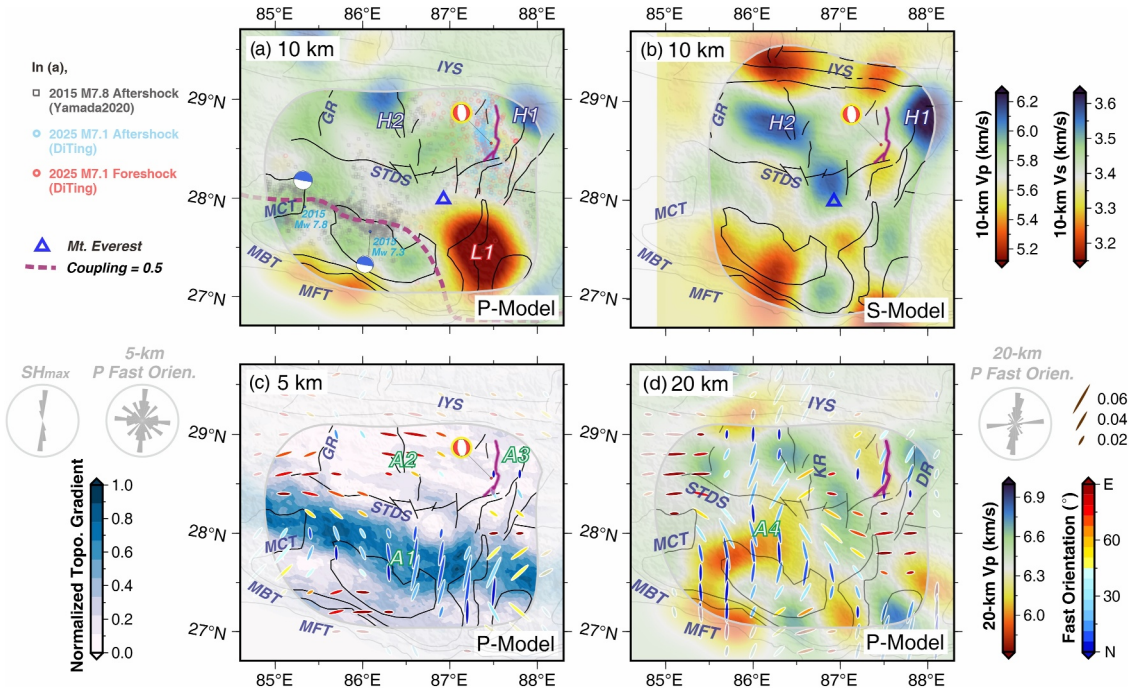

Figure 4. Seismic tomographic images at shallow crustal depths (a–b) 10-km P-wave and S-wave velocities. The purple line represents the contour for Main Himalayan Thrust interseismic coupling degree of 0.5 (Dal Zilio et al., 2020). The earthquake sequences of the M7.1 Dingri and M7.8 Gorkha–Nepal earthquakes are shown as colored dots and squares, respectively (Yamada et al., 2019; M. Zhao et al., 2025). (c) 5-km P-wave azimuthal anisotropy. The fast orientation and anisotropy magnitude are represented by the orientation and direction/color of the bar line, respectively. The background shows the normalized maximum topographic gradients. Rose diagrams for fast orientations and maximum horizontal compressive stresses (SH_{max}; Pietrolungo et al., 2024) are positioned at the left. (d) 20-km P-wave velocity and azimuthal anisotropy. Rose diagram for fast orientations is positioned at the right. The prominent anomalies discussed in the main text are labeled.

In the shallow crust (e.g., 5–10 km depths; Figures 4a–4c), the Dingri earthquake source region is sandwiched between two high-velocity zones (H1, H2), a feature consistently observed in both the Vp and Vs models. The Vp model also reveals a pronounced low-velocity anomaly (L1) in the Higher Himalaya east of ~86.5°E, but is not clearly observed in the Vs model, possibly due to the comparably lower depth resolution of the Vs model and/or the unique seismic response of the local lithology. P-wave azimuthal anisotropy is generally moderate (~3%) at shallow depths and demonstrates explicit north–south variations that transitions from NNE–SSW orientations (SH_{max}-parallel, A1) in the Himalayan piedmont to WNW–ESE orientations (orogen-parallel, A2) in the STDS and farther north. The mainshock rupture initiates to the south of a weakly anisotropic zone (<1%, A3) that corresponds to the Lhagai dome and then propagates through it unilaterally. This A3 anomaly is emphasized in Section 5.1. Similar weakly anisotropic zones are also observed beneath the Qubusang dome and along the STDS between ~86.0°E and ~87.3°E.

At 20-km depth (Figure 4d), P-wave velocity and anisotropy features are moderately correlated (Pearson's correlation coefficient: −0.45; Figure S8d in Supporting Information S1), with low velocity and north–south fast orientations (A4) identified in the Dingri earthquake source region and the Higher Himalaya (~85.5°–87.0°E), while high velocity and east–west fast orientations appear as secondary features and mostly dominate elsewhere. In the mid-crustal levels (e.g., 30-km depth; Figure 5a), a pervasive low-Vs anomaly (3.1–3.3 km/s, L2) underlies the seismogenic fault and extends northwestward to the Indus–Yarlung Suture (IYS). In contrast, a north-dipping high-velocity anomaly (H3) is imaged to the south (Figures 5a and 6c), representing the underthrusting Indian crust beneath the Lesser–Higher Himalaya.

Our Vp and Vs images are generally consistent with previous tomographic models in this region. The L1 anomaly is also visible in the larger-scale Vp models of Li, Pei et al. (2024) (Figure S9a in Supporting Information S1) and Wei and Zhao (2016), though its shape and amplitude differ. Notably, our delineation of this L1 anomaly shows a strong spatial correlation with a zone of reduced seismicity along the Main Himalayan Thrust (MHT) (Figures 3a and 4a). The latter study also identifies dominant north–south P-wave fast orientations in the Himalaya above

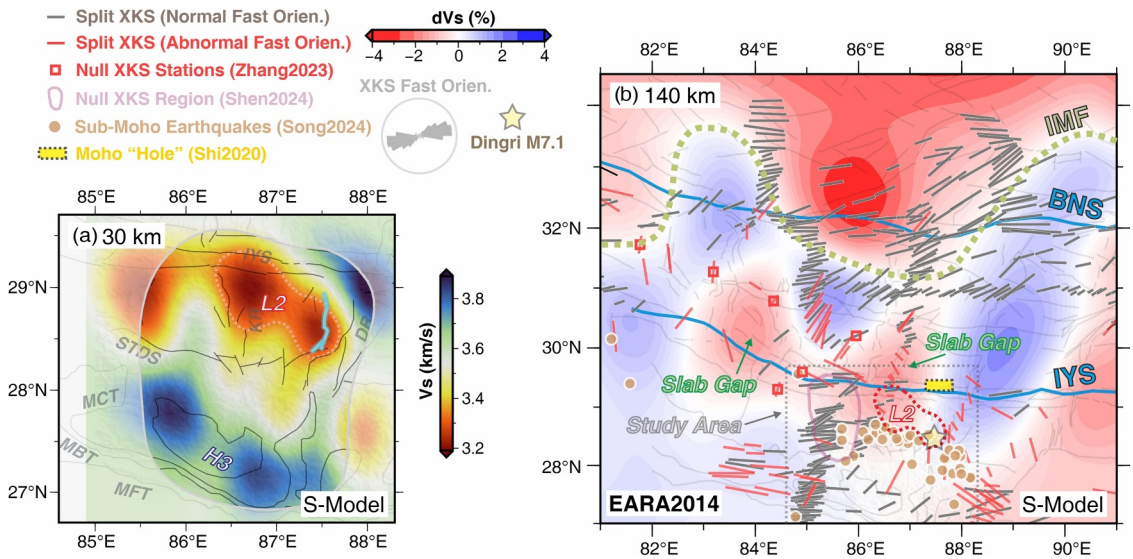

Figure 5. Seismic tomographic images at deep crustal and upper mantle depths. (a) 30-km S-wave velocity. The layout is similar to Figure 4. (b) 140-km S-wave velocity (M. Chen et al., 2017). Split and null XKS measurements (Shen et al., 2024; C. Wu et al., 2019; Wüstefeld et al., 2009; B. Zhang et al., 2023), sub-Moho earthquakes (Song & Klemperer, 2024), and Moho "holes" (Shi et al., 2020) are shown. Split XKS measurements exhibiting anomalous fast orientations that deviates from the regional average (~70°; see rose diagram) by >30° are colored in red. Abbreviations: BNS, Bangong–Nujiang suture; IMF, Indian Mantle Front.

~25-km depth, though the upper boundary of this feature is less well constrained. In addition, we newly detect several low-anisotropy patches in and around the Tethyan Himalaya. At greater depths, the L2 anomaly appears consistent with previous delineations derived from conventional two-step surface-wave inversions (Guo et al., 2009; Lü et al., 2024; Thapa et al., 2023).

In this study, we utilize both body-wave and surface-wave data, which have distinct sensitivities, for tomographic inversions. This combination provides independent yet complementary constraints on the seismogenic environment of this destructive earthquake. The isotropic Vs model also serves as a critical link between geodynamical processes occurring in the shallow crust and in the upper mantle. Further advances can be expected

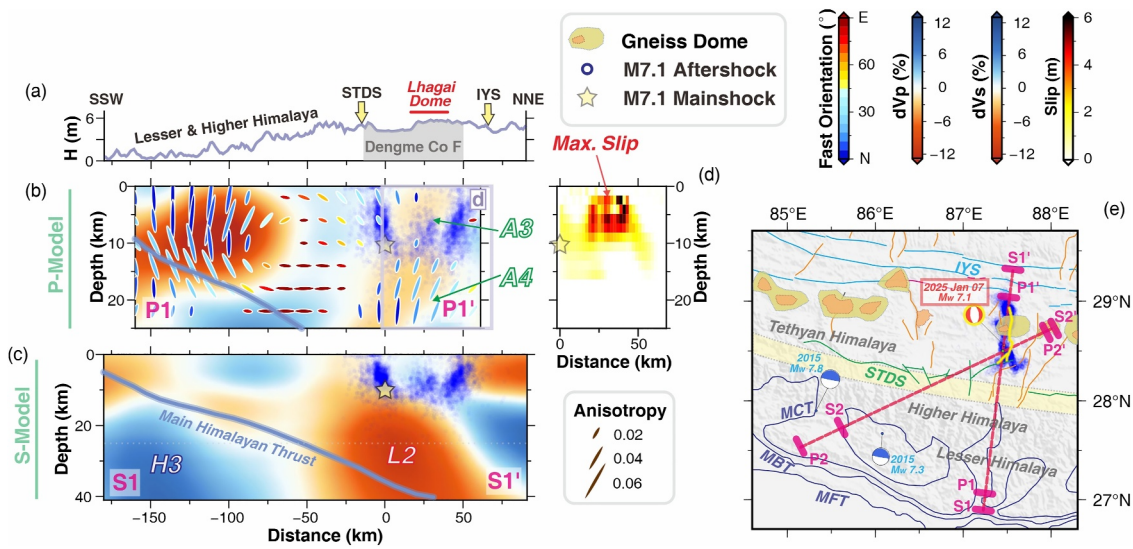

Figure 6. An NNE-trending cross-section of the seismic tomographic models (a–c) Topography, P-wave anisotropic and S-wave isotropic models along the profile (P1–P1′/S1–S1′) that crosses the M7.1 mainshock epicenter. The depth extents for the P-wave and S-wave models are 0–25 and 0–40 km, respectively. The panels are aligned according to the location of the M7.1 mainshock epicenter (yellow star). The Main Himalayan Thrust geometry is from Schulte-Pelkum et al. (2005). The aftershock sequence (Yao et al., 2025) are shown in blue dots. (d) The coseismic slip distribution for the mainshock (Yu et al., 2025). Notably, the high-slip zone for the mainshock rupture corresponds to the A3 anomaly with weak anisotropy. (e) Map view illustrating the cross-section locations and geological features.

from anisotropic inversions of surface-wave data, which could be enabled by the dense rapid-response seismic network deployed after the mainshock and the future anisotropic SurfATT release.

5. Discussion

5.1. Seismogenic Fault Cutting Through Hard Gneiss Dome

Intensive lower-plate crustal anatexis and high-grade metamorphism in ~44–7 Ma have led to the formation of two subparallel leucogranite belts along the STDS and within the Tethyan Himalaya, extending from ~78° to ~92°E (F. Wu et al., 2015). The emplacement of leucogranite plutons in the Tethyan Himalaya takes the form of gneiss domes (i.e., northern Himalayan gneiss domes), where a leucogranite core is encased by an outer shell of deformed gneiss (Figure 1) (e.g., D. Li et al., 2003). These granite-cored gneiss domes serve as tectonic windows into the exhumated Higher Himalayan crystalline, which exhibit higher strength compared to the surrounding weak, low-grade Tethyan Himalayan sedimentary sequence.

The Lhagai dome, which encompasses the northern segment of the Dengme Co fault, is characterized by negligible seismic anisotropy at the shallow depths (<1%, A3; Figures 4c and 6b). This observation can be interpreted to reflect the overall low-angle structural fabrics and less developed fractures there, which indicates that the crystalline rocks beneath the Lhagai dome are highly resistant to deformation under regional stress. Such a stiff tectonic unit therefore represents a high-strength asperity, particularly conducive to high elastic strain buildup and high-magnitude earthquake nucleation (Sun et al., 2022). Notably, the core area of the mainshock rupture zone, where the highest slip occurred (Yu et al., 2025), coincides with the location of this asperity (Figure 6d), providing further evidence for our inference. A similar anisotropy–asperity–rupture association has been documented in the 2013 M_s 7.0 Lushan earthquake source region (Y. Liu et al., 2015).

It has long been recognized that the locations of fault asperities, inferred from detailed rupture process imaging of large earthquakes, may also be revealed by geophysical imaging of structural heterogeneities beforehand. High-velocity and/or high-resistivity anomalies have frequently been observed within high-slip zones of many catastrophic earthquakes worldwide (e.g., the 2015 M_w 7.8 Gorkha–Nepal earthquake, Pei et al., 2016; the 2023 M_w 7.8 and M_w 7.6 Türkiye earthquake doublet, Wang Qiu, et al., 2025; the 2008 M_w 7.9 Wenchuan earthquake, Wang, Wang et al., 2021; G. Zhao et al., 2012; the 2011 M_w 9.0 Tohoku–oki earthquake, Z. Huang & Zhao, 2013; the 2008 M_w 6.9 Iwate–Miyagi Nairiku earthquake, Okada et al., 2012; the 2004 M_w 6.0 Parkfield earthquake, Thurber et al., 2006). In comparison, characteristic seismic anisotropy features in source regions remain insufficiently constrained and thus elusive (Y. Liu et al., 2015; Tong et al., 2021). In this study, we identify a clear association between low anisotropy and fault asperity, which may serve as an additional geophysical indicator for recognizing regions prone to destructive earthquakes. Furthermore, we note that different geophysical indicators do not always converge. In the case of the Dingri earthquake, although the inferred asperity is marked by low anisotropy and high resistivity (Sheng et al., 2023), a clear high-velocity feature for the asperity is absent. This reduced seismic velocities may be attributable to elevated temperatures, as indicated by pronounced low-Vs anomalies at greater depths and the widespread occurrence of hot springs at the surface (Hao, Gang et al., 2024). Therefore, to delineate such high-risk zones more reliably, a multi-parameter geophysical characterization of the fault zones is preferred. Reliance on a single parameter may be problematic due to its sensitivity to multiple factors, whereas an integrated multi-parameter approach can provide complementary insights and reduce interpretational ambiguity.

It is noteworthy that the high-strength characteristic of the Lhagai dome is not unique among the Himalayan leucogranite belts. Within our study region, the Qubusang dome in the northern belt and the central segment of the southern belt along the STDS (~86.0°–87.3°E) also exhibit negligible seismic anisotropy (Figure 4c), suggesting that they may function as tectonic units capable of accumulating high elastic strain. This inference is supported by their similar lithological composition, primarily high-grade metamorphic rocks and leucogranite bodies, which implies comparable rock strength. Seismicity in these areas is relatively low (Figures 3a and 4a), but moderate-magnitude earthquakes have occurred at these locations (Figure 1), highlighting the need for further investigation of potential seismic hazards. In contrast, the Suozuo dome and the southern leucogranite belt west of ~86.0°E and east of ~87.3°E lack such low-anisotropy signatures, possibly due to their smaller spatial extent and/or the influence of localized ramp–duplex structures atop the MHT (See Section 5.4).

Additionally, fluids may have infiltrated the faults within the southern Dinggye Rift zone, where the 2025 M7.1 mainshock rupture initiated and where previous events (including the 2015 M_w 5.8, 2016 M_w 5.3 and 2020 M_w 5.7 earthquakes) also occurred. This inference is supported by the relatively high Vp/Vs ratio (Figure S10 in Supporting Information S1; derived from the depth-averaged P- and S-wave velocity models) and high electrical conductivity (Sheng et al., 2023) reported for the shallow crust in this region. For the southern segment of the Dengme Co fault in particular, potential fluid sources include the deep-crustal melts (See Section 5.2), the Dengme Co lake and the sedimentary layers. As fluid infiltration can effectively reduce the friction coefficient and the effective normal stress on fault planes, it may have played a crucial role in the rupture initiation processes of these earthquakes. Nevertheless, additional direct constraints on Vp/Vs ratios are necessary to further evaluate the scenario of fluid involvement.

5.2. Crustal Partial Melts of Mantle Origin

We propose that the imaged L2 (Figures 5a and 6c), which is widely distributed below 10-km depth in the Tethyan Himalaya, reflects that the Dingri earthquake source region is under the influence of active crustal melting originating from deeper levels. L2 represents the southernmost extension of a broader low-velocity zone previously imaged along the IYS between ~85.5°E and ~89.0°E (S. Huang et al., 2020; Figure S9b in Supporting Information S1). At 30-km depth, the Vs values within the L2 anomaly range from 3.1 to 3.3 km/s, which are considerably lower than laboratory-derived estimates for solid-state major deep-crustal lithologies (e.g., amphibolite, granulite) under comparable pressure–temperature conditions (~3.4–3.6 km/s) (Christensen, 1996). This discrepancy suggests the presence of partial melt in the region. This partial melting scenario is further supported by multiple lines of evidence: (a) geochemical signatures of Miocene-aged leucogranite outcrops above the L2 anomaly that point to past episodes of active magmatism (e.g., Kali et al., 2010; Mitsuishi et al., 2012); (b) geophysical observations of high seismic attenuation (A. F. Sheehan et al., 2014) and high electrical conductivity (Unsworth et al., 2005) that spatially coincide with the L2 anomaly. Using the Gassmann's equation (Chu et al., 2010), we estimate the melt fraction within L2 to be ~6%–9% (See Text S1 in Supporting Information S1 for details). This estimate is broadly consistent with previous assessments of crustal melt fractions in the low-velocity Tibetan crust (typically ranging from 2% to 9%; e.g., Li, He et al., 2024; Nie et al., 2023), though it may be overestimated if aqueous fluids or compositional heterogeneities also contribute to the observed velocity reduction.

The formation of this partially molten crust may be facilitated by the heat and melt transported by asthenospheric upwelling. A comparison between L2 and mantle Vs images (Figure 5b; M. Chen et al., 2017) reveals that L2 overlies a NW–SE-trending band of low-velocity patches embedded within a high-velocity background. This configuration suggests that the northward-underthrusting Indian slab, characterized by high velocity, is not laterally homogeneous. It contains internal gaps, potentially resulting from intrinsic slab weaknesses (Godin & Harris, 2014) and manifested in the form of foundering or tearing, which serve as conduits for localized asthenospheric upwelling. In Figure 5b, we also show that the distribution of anomalous XKS (e.g., SKS, SKKS) fast orientations (red bars) that deviates from the Tibetan average (WSW–ENE; Gray bars) but generally aligns with the bulk-crustal anisotropy direction (NNE–SSW) (B. Zhang et al., 2023) follows the NW–SE-trending mantle low-velocity band. This provides further evidence for the presence of localized asthenospheric upwelling within the Indian slab, where the weak mantle azimuthal anisotropy at the slab window likely results from the near-vertical alignment of olivine α-axis induced by the vertical flow. We further suggest that the Dingri earthquake source region (located above the edge of L2) is likely subject to enhanced Moho-penetrating fluid flow, given the following observations at intra-slab lithospheric steps (i.e., the boundary between high- and low-velocity anomalies in Figure 5b): (a) a clustering of XKS null splitting measurements (Shen et al., 2024; B. Zhang et al., 2023) that implies intense vertical flow, (b) the presence of sub-Moho seismicity (Song & Klemperer, 2024) and the absence of Moho doublet signals (Shi et al., 2020) that indicate downwelling of partially eclogitized Indian lower crust and the penetration of hot mantle-derived fluids into the overlying crust.

5.3. Basal Shear Imposed by the Underthrusting Indian Slab

At high lithostatic pressures, crack-related anisotropy dissipates (Crampin, 1994), making the crystallographic preferred orientation (CPO) of anisotropic minerals the primary mechanism for seismic anisotropy. At 20-km depth, the Himalaya exhibits predominantly north–south-trending P-wave anisotropy, subparallel to the plate convergence direction (A4 anomaly; Figure 4d). Laboratory studies have demonstrated that amphibole, an

abundant constituent mineral in the deep-crust xenoliths from Tibet (Wang, Zhang et al., 2021), can develop shear-subparallel CPO fabrics under simple shear stress and high temperature conditions (Ko & Jung, 2015). This scenario is consistent with the tectonic setting of the Tibetan plateau, where the Indian plate actively underthrusts northward beneath the Eurasia along the MHT. Our observations thus provide direct evidence for the strong, active north–south basal shear strain and stress beneath the Himalaya, including the 2025 Dingri earthquake source region where stress is conveyed to shallower levels through the mechanically coupled (Copley et al., 2011) Himalayan crust.

This implication aligns with our previous studies (B. Zhang et al., 2023; B. Zhang et al., 2025); however, in this study, anelastic basal shear strain south of the STDS is newly revealed, made possible by the improved vertical resolution of P-wave traveltime tomography compared to the receiver-function technique. Notably, the observed north–south anisotropy is correlated with low-velocity anomalies (Figures 4d and Figure S8d in Supporting Information S1), while the low-velocity anomalies generally follow the geometry of the MHT and extend downward to the fluid-rich L2 (Figure 6c). These spatial associations further suggest that the MHT functions not only as a shear zone but also as a conduit for fluid migration contributing to the triggering of MHT earthquakes such as the 2015 M_w 7.8 Gorkha–Nepal earthquake and its M_w 7.3 aftershock (See Figure S11 in Supporting Information S1). The sequences of the Gorkha–Nepal and Dingri earthquakes (dots and squares in Figure 4a), the long-term seismicity (Figure 3a), and the interseismicly high-coupled MHT patches (purple dashed line in Figure 4a; Dal Zilio et al., 2020) all appear to be spatially bounded by the L1 anomaly characterized by low Vp (<5.5 km/s), which likely represents a creeping zone with weak rheology.

5.4. Formation Mechanisms of Shallow-Crustal Anisotropy

Apart from the low-anisotropy areas discussed in Section 5.1, the rest of the study region generally exhibits moderate upper-crustal anisotropy, with an explicit north–south contrast (Figure 4c). The formation mechanisms of seismic anisotropy at these depths are typically stress-related and/or structure-related. Figure S8 in Supporting Information S1 shows that upper-crustal seismic velocity and anisotropy are only weakly correlated (Pearson's correlation coefficient <0.3), indicating that local structural heterogeneities alone, as reflected by velocity variations, cannot fully explain the observed anisotropy. A further comparison between the P-wave fast orientations and the maximum horizontal compressive stress directions (SH_{max}; Pietrolungo et al., 2024) suggests that regional tectonic stress, which alters the aspect-ratio of microcracks openings, is likely the dominant mechanism for anisotropy in the southern Himalaya, where topography is relatively subdued and still rising (Figure 4c). Conversely, in and north of the STDS, where the landscape has evolved into a flat plateau, the P-wave fast orientations deviate from SH_{max} but instead align subparallel to the orogen strike, indicating structural anisotropy (Figure 4c). In other words, the anisotropy in the north can be attributed to the deformed structural fabrics with a high-angle foliation plane produced by north–south compressional folding.

However, it is important to note that the distinct anisotropy-forming mechanisms delineated across the STDS do not preclude the presence of stress-induced anisotropy within the high plateau of the northern Himalaya. The 5-km horizontal slice below sea level corresponds to approximately 10 km below the surface of the northern Himalaya, where elevated lithostatic pressures are expected to reduce microcrack densities relative to regions further south. This implies that the observed anisotropy contrast is primarily influenced by elevation differences and likely reflects depth-dependent strain variations within the upper crust.

Additionally, the orogen-parallel anisotropy observed in the upper crust along the STDS persists to ~20-km depth in regions west of ~85.5°E and east of ~87.0°E (Figure 4d). Just beneath these segments, steeper ramps in the MHT have been identified (Acton et al., 2011; Bai et al., 2019), in contrast to the smoothly deepening MHT geometry observed in the intervening region (Schulte-Pelkum et al., 2005), as revealed by receiver-function and tomographic studies. These MHT ramps are likely sites to facilitate the accretion of lower plate materials into the upper plate, forming a series of high-angle thrust duplexes, as documented by seismic reflection studies (e.g., Gao et al., 2016). Thus, the ramp–duplex scenario may provide a plausible explanation for the deep-seated patches of orogen-parallel anisotropy observed along the STDS.

5.5. A Conceptual Model for the Generation of the M7.1 Dingri Normal-Faulting Earthquake

The structural configurations and active geodynamic processes underlying the Dingri earthquake source region, as discussed in Sections 5.1–5.3, collectively provide valuable insights into the generation of the M7.1 Dingri

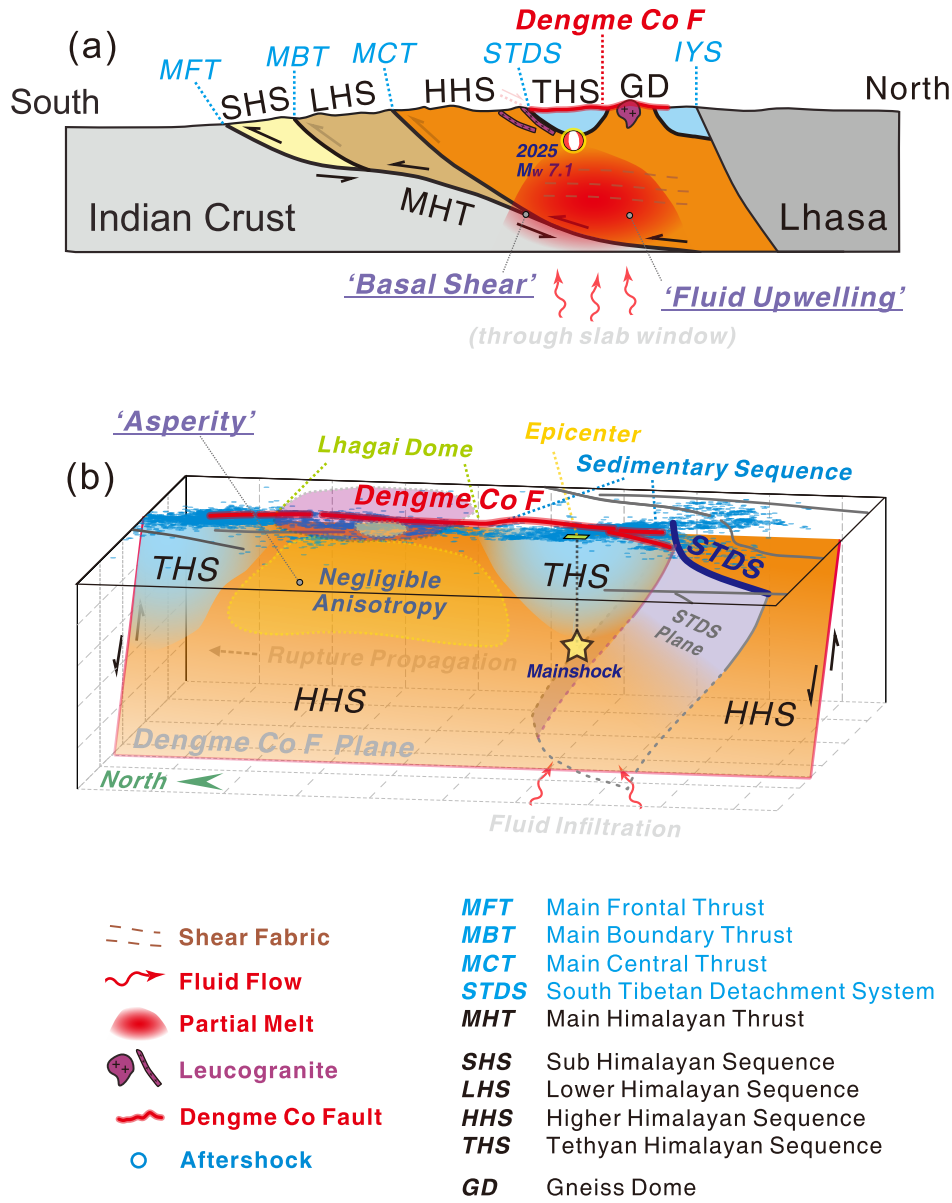

Figure 7. Cartoons illustrating the seismogenic environment of the 2025 M7.1 Dingri earthquake. (a) A regional-scale picture. The northward-advancing Indian crust along the Main Himalayan Thrust exerts north-directed basal shear stresses on the overlying Himalayan crust and induces convergence-parallel shear fabrics within. The upward fluid flow through the Indian slab window causes pronounced crustal partial melting and enhances the local gravitational potential energy through replacement of in situ lithosphere by hot, less dense materials. These tectonic processes have dramatically modified the crustal stress state and are responsible for the normal-faulting focal mechanism. (b) A zoom-in picture on the Dengme Co fault. The high-strength Lhagai dome composed of Higher Himalayan crystalline rocks with leucogranite cores acts as an asperity, which enables the high interseismic strain buildup required for the genesis of an M7.1 earthquake and controls the slip behaviors. Mainshock slip initiates to the south of the asperity and propagates unilaterally through it. Fluid infiltration may have participated in triggering the mainshock. The figures are not to scale.

normal-faulting earthquake. Specifically, we focus on its two puzzling features: (a) the normal-faulting focal mechanism (Figure 7a) and (b) the large earthquake magnitude (Figure 7b).

Firstly, why does normal faulting occur? According to Anderson's fault theory, the types of faulting regime are determined by the orientation of the principal stresses, which in turn are governed by the prevailing tectonic forces. The seismogenic fault is located in the Xainza–Dinggye Rift zone composed of grabens and bounding normal faults (J. Zhang & Guo, 2007). The development of these east–west extensional structures requires a stress

configuration in which the maximum principal stress (σ_1) is vertical and the minimum principal stress (σ_3) is oriented east–west. However, in a compressional orogen such as Tibet, where the ongoing India–Eurasia collision results in strong north–south compression, the σ_1 typically aligns in the north–south direction, favoring thrust faulting as observed at the collision front of the Himalaya. Therefore, the occurrence of normal faulting in the high plateau of Tibet suggests that additional tectonic processes must have contributed to modifying the local stress field, specifically, to counteract the dominant north–south compressional stress. Topographically induced extensional stresses help but cannot accomplish the job alone, as shown by numerical simulations of surface tectonics in Tibet (Copley et al., 2011). Our analyses demonstrate that the basal shear imposed by the underthrusting Indian plate is a prevalent tectonic force acting in the Dinggye Rift zone as well as other southern Tibetan rifts (see Section 5.3). The effect of this basal shear force is to drag the upper plate (Tibet) away from the lower plate (India), which results in north–south extensional stresses. Additionally, the Dinggye Rift zone is featured by localized asthenospheric upwelling through a slab window (see Section 5.2). Such convective removal of mantle lithosphere, in principle, produces excess GPE, causes surface uplift, and consequently increases the topographically induced stresses in the area. As a result, the basal shear and topographically induced stresses enhanced by asthenospheric upwelling, collectively balance the north–south compressional force from the India–Tibet convergence, thereby reconfiguring the local stress field to favor normal faulting.

Secondly, why such a large magnitude? The M7.1 Dingri earthquake is among the world's largest normal-faulting earthquakes in history. Due to the lower yield stresses of lithosphere in extension than in compression, continental normal-faulting earthquakes generally have smaller magnitudes than other fault geometries (Neely & Stein, 2021). To facilitate the nucleation of the M7.1 Dingri earthquake, we speculate that fault structures play a significant role. In Section 5.1, we demonstrate that the seismogenic fault cuts through a high-strength asperity, which manifests as the Lhagai dome at the surface. The effect of the asperity is to make the fault segment therein an interseismically locked patch, thereby enabling the high elastic strain buildup essential for generating large earthquakes (Y. Li et al., 2025). This asperity had remained unbroken and acted as a barrier during preceding earthquakes (e.g., the 2020 M_w 5.7 event), and its eventual failure allowed the 2025 Dingri earthquake to develop into a M_w 7.1 large-scale rupture. The rupture first initiates to the south of the asperity, a complex setting prone to triggering, where the asperity intersects with the weak sedimentary sequence above and the NW-dipping STDS fault plane to the south. It then propagates unilaterally through the asperity, releasing the accumulated strain within and causing the high coseismic slip amount. Aftershocks, as expected, are mainly clustered at the low-slip northern and southern edges of the mainshock rupture zone in response to the increased stress concentration (Aki, 1979).

Additionally, regarding the triggering factors, fluid (including melt) pressurization and infiltration into the southern segment of the Dengme Co fault would reduce the friction coefficient on fault planes and consequently increase the likelihood of fault failure (Wang, Wang et al., 2021). Coulomb failure stress change in the Dingri source region increased by 12 kPa during the 2015 M_w 7.8 Gorkha–Nepal earthquake (C. Liu et al., 2017) and has continued to rise due to its afterslip (Li, Li et al., 2024). Both factors may have contributed to triggering this M7.1 earthquake.

6. Conclusions

In this study, high-resolution P-wave azimuthally anisotropic and S-wave isotropic velocity models of the 2025 Dingri earthquake source region and its surroundings are obtained using adjoint-state traveltime tomography techniques. Our models reveal negligible anisotropy in the upper crust of the source region, convergence-parallel anisotropy in the middle crust, and pronounced low seismic velocities below hypocenter which can be traced to the mantle depths when integrated with mantle tomographic model. These lines of seismological evidence suggest that the generation of this high-magnitude normal-faulting event is controlled by a local high-strength asperity (Lhagai gneiss dome) and the structure and kinematics of the underthrusting Indian slab. To mitigate the risk of similar earthquake disasters in southern Tibet, comprehensive seismic hazard assessment in similar tectonic settings, where north–south-trending rifts intersect with the northern Himalayan gneiss belt, is recommended.

Conflict of Interest

The authors declare no conflicts of interest relevant to this study.

Data Availability Statement

The seismic velocity models obtained in this study are available for download from Tong (2025). The HIMNT data (network code: YL) are archived by the IRIS DMC (A. Sheehan et al., 2001). First-arrival P-wave traveltimes can be partly assessed through J. Li et al. (2024) or fully retrieved along with the Rayleigh-wave traveltimes from B. Zhang (2025). TomoATT and SurfATT packages are freely accessible via J. Chen et al. (2025) and M. Xu et al. (2025), respectively.

Acknowledgments

We are grateful to Shunping Pei for sharing the P-wave traveltime data, Zhenhong Li and Xiaoning Hu for providing the coseismic slip model. This work is funded by Ministry of Education, Singapore, under its MOE AcRF Tier-2 Grant (MOE-T2EP20122-0008 and MOE-T2EP50124-0011). The computational work for this article was partially performed on resources of the National Supercomputing Centre, Singapore (https://www.nscc.sg). The authors thank Editors Rachel Abercrombie and Daoyuan Sun, the Associate Editor, and three anonymous reviewers for their constructive comments, which greatly improved this manuscript.

References

Acton, C. E., Priestley, K., Mitra, S., & Gaur, V. K. (2011). Crustal structure of the darjeeling-sikkim Himalaya and southern Tibet. *Geophysical Journal International*, *184*(2), 829–852. https://doi.org/10.1111/j.1365-246X.2010.04868.x

Aki, K. (1979). Characterization of barriers on an earthquake fault. *Journal of Geophysical Research*, *84*(B11), 6140–6148. https://doi.org/10.1029/JB084iB11p06140

Bai, L., Klemperer, S. L., Mori, J., Karplus, M. S., Ding, L., Liu, H., et al. (2019). Lateral variation of the main Himalayan Thrust controls the rupture length of the 2015 Gorkha earthquake in Nepal. *Science Advances*, *5*(6), eaav0723. https://doi.org/10.1126/sciadv.aav0723

Bao, X., Song, X., & Li, J. (2015). High-resolution lithospheric structure beneath mainland China from ambient noise and earthquake surface-wave tomography. *Earth and Planetary Science Letters*, *417*, 132–141. https://doi.org/10.1016/j.epsl.2015.02.024

Barazangi, M., & Ni, J. (1982). Velocities and propagation characteristics of Pn and Sn beneath the Himalayan arc and Tibetan Plateau: Possible evidence for underthrusting of Indian Continental lithosphere beneath Tibet. *Geology*, *10*(4), 179–185. https://doi.org/10.1130/0091-7613(1982)10<179:vapcop>2.0.co;2

Bensen, G. D., Ritzwoller, M. H., Barmin, M. P., Levshin, A. L., Lin, F., Moschetti, M. P., et al. (2007). Processing seismic ambient noise data to obtain reliable broad-band surface wave dispersion measurements. *Geophysical Journal International*, *169*(3), 1239–1260. https://doi.org/10.1111/j.1365-246X.2007.03374.x

Bian, S., Gong, J., Zuza, A. V., Yang, R., Chen, L., Ji, J., et al. (2022). Along-strike variation in the initiation timing of the north-trending rifts in southern Tibet as revealed from the Yadong-gulu rift. *Tectonics*, *41*(7), e2021TC007091. https://doi.org/10.1029/2021tc007091

Bischoff, S. H., & Flesch, L. M. (2018). Normal faulting and viscous buckling in the Tibetan Plateau induced by a weak lower crust. *Nature Communications*, *9*(1), 4952. https://doi.org/10.1038/s41467-018-07312-9

Chen, J., Chen, G., Nagaso, M., & Tong, P. (2023). Adjoint-state traveltime tomography for azimuthally anisotropic media in spherical coordinates. *Geophysical Journal International*, *234*(1), 712–736. https://doi.org/10.1093/gji/ggad093

Chen, J., Nagaso, M., Xu, M., & Tong, P. (2025). TomoATT: An open-source package for Eikonal equation-based adjoint-state traveltime tomography for seismic velocity and azimuthal anisotropy. *Computers and Geosciences*, *204*, 105995. https://doi.org/10.1016/j.cageo.2025.105995

Chen, M., Niu, F., Tromp, J., Lenardic, A., Lee, C.-T. A., Cao, W., & Ribeiro, J. (2017). Lithospheric foundering and underthrusting imaged beneath Tibet. *Nature Communications*, *8*, 15659. https://doi.org/10.1038/ncomms15659

Christensen, N. I. (1996). Poisson's ratio and crustal seismology. *Journal of Geophysical Research*, *101*(B2), 3139–3156. https://doi.org/10.1029/95jb03446

Chu, R., Helmberger, D. V., Sun, D., Jackson, J. M., & Zhu, L. (2010). Mushy magma beneath Yellowstone. *Geophysical Research Letters*, *37*(1), L01306. https://doi.org/10.1029/2009GL041656

Copley, A., Avouac, J.-P., & Wernicke, B. P. (2011). Evidence for mechanical coupling and strong Indian lower crust beneath southern Tibet. *Nature*, *472*(7341), 79–81. https://doi.org/10.1038/nature09926

Crampin, S. (1994). The fracture criticality of crustal rocks. *Geophysical Journal International*, *118*(2), 428–438. https://doi.org/10.1111/j.1365-246x.1994.tb03974.x

Dal Zilio, L., Jolivet, R., & van Dinther, Y. (2020). Segmentation of the main himalayan Thrust illuminated by Bayesian inference of interseismic coupling. *Geophysical Research Letters*, *47*(4), e2019GL086424. https://doi.org/10.1029/2019gl086424

England, P., & Houseman, G. (1989). Extension during Continental convergence, with application to the Tibetan Plateau. *Journal of Geophysical Research*, *94*(B12), 17561–17579. https://doi.org/10.1029/jb094ib12p17561

England, P., & Molnar, P. (1993). Cause and effect among thrust and normal faulting, anatectic melting and exhumation in the Himalaya. *Geological Society, London, Special Publications*, *74*, 401–411. https://doi.org/10.1144/GSL.SP.1993.074.01.27

Fan, Y., Zhang, J., Lin, C., Wang, X., & Zhang, B. (2021). Miocene granitic magmatism constrains the early E-W extension in the Himalayan orogen: A case study of Kung Co leucogranite. *Lithos*, *398–399*, 106295. https://doi.org/10.1016/j.lithos.2021.106295

Gao, R., Lu, Z., Klemperer, S. L., Wang, H., Dong, S., Li, W., & Li, H. (2016). Crustal-scale duplexing beneath the yarlung Zangbo suture in the western Himalaya. *Nature Geoscience*, *9*, 555–560. https://doi.org/10.1038/ngeo2730

Godin, L., & Harris, L. B. (2014). Tracking basement cross-strike discontinuities in the Indian crust beneath the Himalayan orogen using gravity data – Relationship to upper crustal faults. *Geophysical Journal International*, *198*(1), 198–215. https://doi.org/10.1093/gji/ggu131

Guo, Z., Gao, X., Yao, H., Li, J., & Wang, W. (2009). Midcrustal low-velocity layer beneath the central Himalaya and southern Tibet revealed by ambient noise array tomography. *Geochemistry, Geophysics, Geosystems*, *10*(5), Q05007. https://doi.org/10.1029/2009GC002458

Hager, C., Stockli, D. F., Dewane, T. J., Gehrels, G., & Ding, L. (2009). Anatomy and crustal evolution of the central Lhasa terrane (S-Tibet) revealed by investigations in the xainza rift. In *EGU General assembly 2009*.

Hao, S., Chen, J., Xu, M., & Tong, P. (2024a). Topography-incorporated adjoint-state surface wave traveltime tomography: Method and a case study in Hawaii. *Journal of Geophysical Research: Solid Earth*, *129*(1), e2023JB027454. https://doi.org/10.1029/2023JB027454

Hao, Y., Gong, Q., Kuang, X., Feng, Y., Zhou, H., & Zheng, C. (2024b). Degassing of mantle-derived helium from hot springs along the India-Asia continental collision settings: Origins, migration velocity and flux. *Geochemistry, Geophysics, Geosystems*, *25*(2), e2023GC011297. https://doi.org/10.1029/2023GC011297

Hodges, K. V. (2000). Tectonics of the himalaya and southern Tibet from two perspectives. *GSA Bulletin*, *112*(3), 324–350. https://doi.org/10.1130/0016-7606(2000)112<324:TOTHAS>2.0.CO;2

Huang, S., Yao, H., Lu, Z., Tian, X., Zheng, Y., Wang, R., et al. (2020). High-resolution 3-D shear wave velocity model of the Tibetan Plateau: Implications for crustal deformation and porphyry Cu deposit formation. *Journal of Geophysical Research: Solid Earth*, *125*(7), e2019JB019215. https://doi.org/10.1029/2019jb019215

Huang, Z., & Zhao, D. (2013). Mechanism of the 2011 Tohoku-oki earthquake (Mw 9.0) and tsunami: Insight from seismic tomography. *Journal of Asian Earth Sciences*, *70–71*, 160–168. https://doi.org/10.1016/j.jseaes.2013.03.010

Kali, E., Leloup, P. H., Arnaud, N., Mahéo, G., Liu, D., Boutonnet, E., et al. (2010). Exhumation history of the deepest central Himalayan rocks, Ama drime range: Key pressure-temperature-deformation-time constraints on orogenic models. *Tectonics*, *29*(2), TC2014. https://doi.org/10.1029/2009tc002551

Kissling, E., Ellsworth, W. L., Eberhart-Phillips, D., & Kradolfer, U. (1994). Initial reference models in local earthquake tomography. *Journal of Geophysical Research*, *99*(B10), 19635–19646. https://doi.org/10.1029/93JB03138

Klein, F. W. (2002). *User's guide to HYPOINVERSE-2000, a Fortran program to solve for earthquake locations and magnitudes* (pp. 2002–2171). U.S. Geological Survey. https://doi.org/10.3133/ofr02171

Ko, B., & Jung, H. (2015). Crystal preferred orientation of an amphibole experimentally deformed by simple shear. *Nature Communications*, *6*, 6586. https://doi.org/10.1038/ncomms7586

Li, D., Liu, D., Liao, Q. a., Zhang, X., & Yuan, Y. (2003). Definition and significance of the Lhagoi Kangri metamorphic core complexes in Sa'gya, southern Tibet. *Geological Bulletin of China*, *22*(5), 303–307.

Li, J., Pei, S., Sun, Q., Liu, H., Liu, W., Hua, Q., & Li, L. (2024a). Oblique rifting in the southern Tibetan Plateau revealed from 3-D high-resolution seismic travel-time tomography around the India–Eurasia continental collision zone. *Journal of Geophysical Research: Solid Earth*, *129*(12), e2024JB029447. https://doi.org/10.1029/2024JB029447

Li, J., & Song, X. (2018). Tearing of Indian mantle lithosphere from high-resolution seismic images and its implications for lithosphere coupling in southern Tibet. *Proceedings of the National Academy of Sciences of the United States of America*, *115*(33), 8296–8300. https://doi.org/10.1073/pnas.1717258115

Li, L., Yao, D., Meng, X., Peng, Z., & Wang, B. (2017). Increasing seismicity in southern Tibet following the 2015 Mw 7.8 Gorkha, Nepal earthquake. *Tectonophysics*, *714–715*, 62–70. https://doi.org/10.1016/j.tecto.2016.08.008

Li, Q., Li, C., Zhao, B., Huang, Y., Wan, Y. T., Kai, & Dong, Q. (2024b). Estimated seismic source parameters for 2020 dingri Mw5.6 earthquake in Xizang and study on the stress triggering. *Chinese Journal of Geophysics*, *67*(1), 172–188.

Li, W., He, R., Yuan, X., Schneider, F., Tilmann, F., Guo, Z., & Chen, Y. J. (2024c). Correlated crustal and mantle melting documents proto-Tibetan Plateau growth. *National Science Review*, *11*(9), nwae257. https://doi.org/10.1093/nsr/nwae257

Li, Y., Shan, X., Qu, C., Zhang, G., Wang, X., & Xiong, H. (2025). Slip deficit rate and seismic potential on crustal faults in Tibet. *Geophysical Research Letters*, *52*(1), e2024GL112122. https://doi.org/10.1029/2024GL112122

Liang, X., Chu, Y., Wan, B., Chen, L., Chen, L., Sandvol, E., et al. (2023). Fragmentation of continental subduction is ending the Himalayan orogeny. *Science Bulletin*, *68*(23), 3048–3054. https://doi.org/10.1016/j.scib.2023.10.017

Liu, C., Dong, P., & Shi, Y. (2017). Stress change from the 2015 Mw 7.8 Gorkha earthquake and increased hazard in the southern Tibetan Plateau. *Physics of the Earth and Planetary Interiors*, *267*, 1–8. https://doi.org/10.1016/j.pepi.2017.04.002

Liu, Y., Zhang, H., Zhang, X., Pei, S., An, M., & Dong, S. (2015). Anisotropic upper crust above the aftershock zone of the 2013 Ms 7.0 Lushan earthquake from the shear wave splitting analysis. *Geochemistry, Geophysics, Geosystems*, *16*(10), 3679–3696. https://doi.org/10.1002/2015GC005972

Lü, Z., Lei, J., Kong, Q., Liu, Q., & Sun, J. (2024). Seismic structure of the 2015 M(w)7.8 gorkha earthquake revealed by ambient seismic noise and teleseismic surface wave tomography. *Scientific Reports*, *14*(1), 7921. https://doi.org/10.1038/s41598-024-57713-8

Ma, J., Song, X., Bunge, H.-P., Fichtner, A., & Tian, Y. (2025). Wholesale flat subduction of the Indian slab and northward mantle convective flow: Plateau growth and driving force of the India-Asia collision. *Proceedings of the National Academy of Sciences of the United States of America*, *122*(7), e2411776122. https://doi.org/10.1073/pnas.2411776122

McCaffrey, R., & Nabelek, J. (1998). Role of oblique convergence in the active deformation of the Himalayas and southern Tibet Plateau. *Geology*, *26*(8), 691–694. https://doi.org/10.1130/0091-7613(1998)026<0691:roocit>2.3.co;2

Mitsuishi, M., Wallis, S. R., Aoya, M., Lee, J., & Wang, Y. (2012). E-W extension at 19 Ma in the Kung Co area, S. Tibet: Evidence for contemporaneous E-W and N-S extension in the Himalayan orogen. *Earth and Planetary Science Letters*, *325–326*, 10–20. https://doi.org/10.1016/j.epsl.2011.11.013

Mohanty, D. D. (2023). Source localized modelling to estimate the depth of anisotropy beneath eastern Himalaya using spatial coherency of shear-wave splitting parameters. *Physics of the Earth and Planetary Interiors*, *336*, 106987. https://doi.org/10.1016/j.pepi.2023.106987

Neely, J. S., & Stein, S. (2021). Why do continental normal fault earthquakes have smaller maximum magnitudes? *Tectonophysics*, *809*, 228854. https://doi.org/10.1016/j.tecto.2021.228854

Nie, S., Tian, X., Liang, X., & Wan, B. (2023). Less-well-developed crustal channel-flow in the central Tibetan Plateau revealed by receiver function and surface wave joint inversion. *Journal of Geophysical Research: Solid Earth*, *128*(4), e2022JB025747. https://doi.org/10.1029/2022jb025747

Okada, T., Umino, N., & Hasegawa, A. (2012). Hypocenter distribution and heterogeneous seismic velocity structure in and around the focal area of the 2008 Iwate-Miyagi nairiku Earthquake, NE Japan—Possible seismological evidence for a fluid driven compressional inversion earthquake. *Earth Planets and Space*, *64*, 717–728. https://doi.org/10.5047/eps.2012.03.005

Pavlis, G. L., & Vernon, F. L. (2010). Array processing of teleseismic body waves with the US Array. *Computers and Geosciences*, *36*(7), 910–920. https://doi.org/10.1016/j.cageo.2009.10.008

Pei, S., Liu, H., Bai, L., Liu, Y., & Sun, Q. (2016). High-resolution seismic tomography of the 2015 Mw7.8 Gorkha earthquake, Nepal: Evidence for the crustal tearing of the Himalayan rift. *Geophysical Research Letters*, *43*(17), 9045–9052. https://doi.org/10.1002/2016GL069808

Pietrolungo, F., Lavecchia, G., Madarieta-Txurruka, A., Sparacino, F., Srivastava, E., Cirillo, D., et al. (2024). Comparison of crustal stress and strain fields in the Himalaya–Tibet region: Geodynamic implications. *Remote Sensing*, *16*(24), 4765. https://doi.org/10.3390/rs16244765

Ruan, Y., Lei, W., Modrak, R., Örsvuran, R., Bozdağ, E., & Tromp, J. (2019). Balancing unevenly distributed data in seismic tomography: A global adjoint tomography example. *Geophysical Journal International*, *219*(2), 1225–1236. https://doi.org/10.1093/gji/ggz356

Schulte-Pelkum, V., Monsalve, G., Sheehan, A., Pandey, M. R., Sapkota, S., Bilham, R., & Wu, F. (2005). Imaging the Indian subcontinent beneath the Himalaya. *Nature*, *435*(7046), 1222–1225. https://doi.org/10.1038/nature03678

Sheehan, A., Wu, F., & Bilham, R. (2001). Himalayan seismotectonics, Nepal and Tibet [Dataset]. *International Federation of Digital Seismograph Networks*. https://doi.org/10.7914/SN/YL_2001

Sheehan, A. F., de la Torre, T. L., Monsalve, G., Abers, G. A., & Hacker, B. R. (2014). Physical state of Himalayan crust and uppermost mantle: Constraints from seismic attenuation and velocity tomography. *Journal of Geophysical Research: Solid Earth*, *119*(1), 567–580. https://doi.org/10.1002/2013jb010601

Shen, C., Gao, S. S., Kong, F., & Liu, K. H. (2024). Tectonic implications of seismic anisotropy layering beneath the southern Tibetan Plateau revealed by integrated shear wave splitting and receiver function analyses. *Journal of Geophysical Research: Solid Earth*, *129*(8), e2024JB029268. https://doi.org/10.1029/2024JB029268

Sheng, Y., Jin, S., Comeau, M. J., Hou, Z., Zhang, L., Wei, W., & Ye, G. (2023). Relationship between the migration of crustal material, normal faulting, and gneiss domes in the vicinity of the Dinggye region, central part of the Tethys–Himalaya terrane: Insights from the 3-D electrical structure. *Tectonophysics*, *869*, 230100. https://doi.org/10.1016/j.tecto.2023.230100

Shi, D., Klemperer, S. L., Shi, J., Wu, Z., & Zhao, W. (2020). Localized foundering of Indian lower crust in the India-Tibet collision zone. *Proceedings of the National Academy of Sciences of the United States of America*, *117*(40), 24742–24747. https://doi.org/10.1073/pnas.2000015117

Song, X., & Klemperer, S. L. (2024). Numerous Tibetan lower-crustal and upper-mantle earthquakes, detected by Sn/Lg ratios, suggest crustal delamination or drip tectonics. *Earth and Planetary Science Letters*, *626*, 118555. https://doi.org/10.1016/j.epsl.2023.118555

Sun, Q., Pei, S., Guo, Z., & Chen, Y. (2022). Structure-controlled asperity on the generation of large earthquakes. *Reviews of Geophysics and Planetary Physics*, *53*(2), 138–147.

Thapa, H. R., Pachhai, S., Aoudia, A., Manu-Marfo, D., Priestley, K., & Mitra, S. (2023). The main Himalayan Thrust beneath Nepal and southern Tibet illuminated by seismic ambient noise and teleseismic P wave coda autocorrelation. *Journal of Geophysical Research: Solid Earth*, *128*(8), e2022JB026195. https://doi.org/10.1029/2022JB026195

Thurber, C., Zhang, H., Waldhauser, F., Hardebeck, J., Michael, A., & Eberhart-Phillips, D. (2006). Three-dimensional compressional wavespeed model, earthquake relocations, and focal mechanisms for the Parkfield, California, region. *Bulletin of the Seismological Society of America*, *96*(4B), S38–S49. https://doi.org/10.1785/0120050825

Tong, P. (2021). Adjoint-state traveltime tomography for azimuthally anisotropic media and insight into the crustal structure of central California near parkfield. *Journal of Geophysical Research: Solid Earth*, *126*(10), e2021JB022365. https://doi.org/10.1029/2021jb022365

Tong, P. (2025). Replication data for: Crustal structure and seismogenic environment for the January 2025 Mw 7.1 Southern Tibet (dingri) earthquake [Dataset]. *DR-NTU (Data)*. https://doi.org/10.21979/N9/TFANS1

Tong, P., Li, T., Chen, J., & Nagaso, M. (2024). Adjoint-state differential arrival time tomography. *Geophysical Journal International*, *236*(1), 139–160. https://doi.org/10.1093/gji/ggad416

Tong, P., Yao, J., Liu, Q., Li, T., Wang, K., Liu, S., et al. (2021). Crustal rotation and fluids: Factors for the 2019 Ridgecrest earthquake sequence? *Geophysical Research Letters*, *48*(3), e2020GL090853. https://doi.org/10.1029/2020GL090853

Unsworth, M. J., Jones, A. G., Wei, W., Marquis, G., Gokarn, S. G., Spratt, J. E., et al. (2005). Crustal rheology of the Himalaya and Southern Tibet inferred from magnetotelluric data. *Nature*, *438*(7064), 78–81. https://doi.org/10.1038/nature04154

Waldhauser, F., & Ellsworth, W. L. (2000). A double-difference earthquake location algorithm: Method and application to the northern Hayward fault, California. *Bulletin of the Seismological Society of America*, *90*(6), 1353–1368. https://doi.org/10.1785/0120000006

Wang, M., & Shen, Z. K. (2020). Present-day crustal deformation of Continental China derived from GPS and its tectonic implications. *Journal of Geophysical Research: Solid Earth*, *125*(2), e2019JB018774. https://doi.org/10.1029/2019JB018774

Wang, N., Li, Y., Shen, W., Jiang, W., Li, Q., & Jiao, Q. (2025a). Source parameters and rapid simulation of strong ground motion of the Ms6.8 earthquake on January 7, 2025 in Dingri (Xizang, China) derived from InSAR observation. *Geomatics and Information Science of Wuhan University*, *50*(2), 404–411.

Wang, X., Zhang, J., Tommasi, A., Jing, Z., & Yuan, M. (2021a). Microstructure and seismic properties of amphibole-rich rocks from the deep crust in southern Tibet. *Tectonophysics*, *811*, 228869. https://doi.org/10.1016/j.tecto.2021.228869

Wang, Z., Qiu, Q., Fu, Y., Lin, J., & Pei, S. (2025b). Distinct triggering mechanisms of the 2023 Türkiye earthquake doublet. *Communications Earth and Environment*, *6*, 287. https://doi.org/10.1038/s43247-025-02266-5

Wang, Z., Wang, J., & Yang, X. (2021b). The role of fluids in the 2008 Ms8.0 Wenchuan earthquake, China. *Journal of Geophysical Research: Solid Earth*, *126*(2), e2020JB019959. https://doi.org/10.1029/2020JB019959

Wei, W., & Zhao, D. (2016). Tomography of the source zone of the 2015 M 7.8 Nepal earthquake. *Physics of the Earth and Planetary Interiors*, *253*, 58–63. https://doi.org/10.1016/j.pepi.2016.01.008

Wu, C., Tian, X., Xu, T., Liang, X., Chen, Y., Taylor, M., et al. (2019). Deformation of crust and upper mantle in central Tibet caused by the northward subduction and slab tearing of the Indian lithosphere: New evidence based on shear wave splitting measurements. *Earth and Planetary Science Letters*, *514*, 75–83. https://doi.org/10.1016/j.epsl.2019.02.037

Wu, F., Liu, Z., Liu, X., & Ji, W. (2015). Himalayan leucogranite: Petrogenesis and implications to orogenesis and Plateau uplift. *Acta Petrologica Sinica*, *31*(1), 1–36.

Wüstefeld, A., Bokelmann, G., Barruol, G., & Montagner, J.-P. (2009). Identifying global seismic anisotropy patterns by correlating shear-wave splitting and surface-wave data. *Physics of the Earth and Planetary Interiors*, *176*(3–4), 198–212. https://doi.org/10.1016/j.pepi.2009.05.006

Xu, M., Hao, S., Chen, J., Zhang, B., & Tong, P. (2025a). SurfATT: High-performance package for adjoint-state surface-wave travel-time tomography. *Seismological Research Letters*. https://doi.org/10.1785/0220240206

Xu, X., Wang, S., Cheng, J., & Wu, X. (2025b). Shaking the Tibetan Plateau: Insights from the Mw 7.1 dingri earthquake and its implications for active fault mapping and disaster mitigation. *npj Natural Hazards*, *2*, 16. https://doi.org/10.1038/s44304-025-00074-7

Yamada, M., Kandel, T., Tamaribuchi, K., & Ghosh, A. (2019). 3D fault structure inferred from a refined aftershock catalog for the 2015 Gorkha earthquake in Nepal. *Bulletin of the Seismological Society of America*, *110*(1), 26–37. https://doi.org/10.1785/0120190075

Yang, Y., Ritzwoller, M. H., Zheng, Y., Shen, W., Levshin, A. L., & Xie, Z. (2012). A synoptic view of the distribution and connectivity of the mid-crustal low velocity zone beneath Tibet. *Journal of Geophysical Research*, *117*(B4), B04303. https://doi.org/10.1029/2011jb008810

Yao, J., Yao, D., Chen, F., Zhi, M., Sun, L., & Wang, D. (2025). A preliminary catalog of early aftershocks following the 7 January 2025 Ms6.8 dingri, Xizang earthquake. *Journal of Earth Sciences*. https://doi.org/10.1007/s12583-025-0210-9

Yu, C., Li, Z., Hu, X., Song, C., Li, S., Liu, H., et al. (2025). Source characteristics and induced hazards of the 2025 M6.8 dingri earthquake, Xizang, China, revealed by imaging geodesy. *Journal of Earth Sciences*, *36*(2), 847–851. https://doi.org/10.1007/s12583-025-0175-8

Zeng, L., Gao, L.-E., Xie, K., & Liu-Zeng, J. (2011). Mid-Eocene high Sr/Y granites in the Northern Himalayan Gneiss domes: Melting thickened lower continental crust. *Earth and Planetary Science Letters*, *303*(3–4), 251–266. https://doi.org/10.1016/j.epsl.2011.01.005

Zhang, B. (2025). Seismic velocity models for the source region of the January 2025 Mw 7.1 southern Tibet (dingri) earthquake [Dataset]. *Zenodo*. https://doi.org/10.5281/zenodo.17044349

Zhang, B., Bao, X., Wu, Y., Jiang, M., & Zhou, K. (2025). Indian crustal front beneath Tibet inferred from seismic anisotropy. *Seismological Research Letters*, *96*(1), 449–460. https://doi.org/10.1785/0220240103

Zhang, B., Bao, X., Wu, Y., Xu, Y., & Yang, W. (2023). Southern Tibetan rifting since late Miocene enabled by basal shear of the underthrusting Indian lithosphere. *Nature Communications*, *14*(1), 2565. https://doi.org/10.1038/s41467-023-38296-w

Zhang, J., & Guo, L. (2007). Structure and geochronology of the southern Xainza-dinggye rift and its relationship to the south Tibetan detachment system. *Journal of Asian Earth Sciences*, *29*(5–6), 722–736. https://doi.org/10.1016/j.jseaes.2006.05.003

Zhang, M., Ellsworth, W. L., & Beroza, G. C. (2019). Rapid earthquake association and location. *Seismological Research Letters*, *90*(6), 2276–2284. https://doi.org/10.1785/0220190052

Zhang, M., Liu, M., Feng, T., Wang, R., & Zhu, W. (2022). LOC-FLOW: An end-to-end machine learning-based high-precision earthquake location workflow. *Seismological Research Letters*, *93*(5), 2426–2438. https://doi.org/10.1785/0220220019

Zhao, G., Unsworth, M. J., Zhan, Y., Wang, L., Chen, X., Jones, A. G., et al. (2012). Crustal structure and rheology of the Longmenshan and wenchuan Mw 7.9 earthquake epicentral area from magnetotelluric data. *Geology*, *40*(12), 1139–1142. https://doi.org/10.1130/G33703.1

Zhao, H. (2004). A fast sweeping method for eikonal equations. *Mathematics of Computation*, *74*(250), 603–627. https://doi.org/10.1090/S0025-5718-04-01678-3

Zhao, M., Xiao, Z., & Chen, S. (2025). *Xizang Dingri M6.8 DiTing model single-station earthquake catalog*, edited.

Zhu, W., & Beroza, G. C. (2018). PhaseNet: A deep-neural-network-based seismic arrival time picking method. *Geophysical Journal International*, *216*(1), 261–273. https://doi.org/10.1093/gji/ggy423

References From the Supporting Information

Christensen, N. I., & Mooney, W. D. (1995). Seismic velocity structure and composition of the Continental crust: A global view. *Journal of Geophysical Research*, *100*(B6), 9761–9788. https://doi.org/10.1029/95JB00259

Rivers, M. L., & Carmichael, I. S. E. (1987). Ultrasonic studies of silicate melts. *Journal of Geophysical Research*, *92*(B9), 9247–9270. https://doi.org/10.1029/JB092iB09p09247

van der Molen, I., & Paterson, M. S. (1979). Experimental deformation of partially-melted granite. *Contributions to Mineralogy and Petrology*, *70*, 299–318. https://doi.org/10.1007/BF00375359

Wang, G., Thybo, H., & Artemieva, I. M. (2021). No mafic layer in 80 km thick Tibetan crust. *Nature Communications*, *12*(1), 1069. https://doi.org/10.1038/s41467-021-21420-z

Erratum

The originally published version of this article omitted a grant number from the Acknowledgments. The following has been added to the Acknowledgments: "This work is funded by Ministry of Education, Singapore, under its MOE AcRF Tier-2 Grant (MOE-T2EP20122-0008 and MOE-T2EP50124-0011)." This may be considered the authoritative version of record.